

Revealing quantum geometry effects in magic angle twisted bilayer graphene using the circular photogalvanic effect

Eylon Persky,^{1,2,3,*} Léonie Parisot,¹ Minhao He,⁴ Jiaqi Cai,⁴ Takashi Taniguchi,⁵ Kenji Watanabe,⁶

Pierre A. Pantaleón,⁷ Francisco Guinea,^{7,8} Xiaodong Xu,⁴ and Aharon Kapitulnik^{1,2,3,9}

¹*Geballe Laboratory for Advanced Materials, Stanford University, Stanford, CA 94305, USA*

²*Stanford Institute for Materials and Energy Sciences,*

SLAC National Accelerator Laboratory, 2575 Sand Hill Road, Menlo Park, CA 94025, USA

³*Department of Applied Physics, Stanford University, Stanford, CA 94305, USA*

⁴*Department of Physics, University of Washington, Seattle, Washington, 98195, USA*

⁵*Research Center for Materials Nanoarchitectonics,*

National Institute for Materials Science, 1-1 Namiki, Tsukuba 305-0044, Japan

⁶*Research Center for Electronic and Optical Materials,*

National Institute for Materials Science, 1-1 Namiki, Tsukuba 305-0044, Japan

⁷*Imdea Nanoscience, Faraday 9, 28047 Madrid, Spain*

⁸*Donostia International Physics Center, Paseo Manuel de Lardizábal 4, 20018 San Sebastián, Spain*

⁹*Department of Physics, Stanford University, Stanford, CA 94305, USA*

(Dated: June 5, 2026)

We report a photocurrent studies of a magic angle twisted bilayer graphene device using near infrared light. Through photocurrent imaging and polarization dependence, we separate the photothermoelectric effect from the photogalvanic effect. We observe a circular photogalvanic effect (CPGE) over a wide range of doping and temperature. The CPGE at normal incidence constraints the symmetry of the system to C_1 , and points to a Berry curvature dipole, in agreement with theoretical predictions for strained graphene. Remarkably, the CPGE vanishes for filling $-2.5 < \nu < -1.5$, suggesting an additional symmetry breaking in that regime. Insight into this effect is obtained through Berry curvature dipole calculations, which emphasize a novel symmetry breaking effect near $\nu = -2$.

INTRODUCTION

The circular photogalvanic effect (CPGE), where circularly polarized light drives a dc current that reverses with helicity, is an exquisitely sensitive probe to the interplay between quantum geometry, strong correlations, and broken symmetries in quantum materials. Thus, CPGE experiments can uncover several frontiers of condensed-matter physics, particularly associated with two-dimensional (2D) heterostructures such as twist-stacked moiré materials.

Focusing on Magic Angle Twisted Bilayer Graphene, CPGE provides a relatively direct probe of valley polarization, Berry curvature, and chiral optical selection rules - quantities that are otherwise hard to access. First, the flat bands and strong interactions present in MATBG are expected to amplify nonlinear optical responses like CPGE, enabling stronger photocurrents at lower optical power than in more conventional 2D materials. Since CPGE is forbidden in centrosymmetric systems, it is a sensitive probe to study many of the symmetry-broken electronic states in MATBG devices, including spontaneous inversion symmetry breaking, nematic order, valley polarization effects and time-reversal symmetry breaking, all can be mapped as function of density, temperature, and displacement field. CPGE couples directly to Berry curvature distribution in momentum space and thus provides experimental access to valley-selective excitation, Berry curvature dipole moments as well as to

orbital magnetic moments. It can therefore reveal the orbital and real-space character of wave-functions, helping discriminate between competing theoretical models of MATBG's insulating and superconducting phases adding information that complements but goes beyond what conventional transport can provide [1, 2]

In this paper we present results of normal-incidence CPGE measurements using 1550 nm light, on a previously studied [3, 4] WSe₂-capped MATBG device, as a function of band-filling. While this excitation is above the characteristic low-energy scale of the flat bands in MATBG and thus expected to be dominated by inter-band photogalvanic mechanisms, the strong correspondence between the CPGE data and the moiré filling and the close tracking the Berry curvature dipole calculated around the Fermi surface, strongly suggest substantial contribution from the moiré electronic structure and the associated quantum geometric properties, which is further rationalized by the high cleanliness of the sample leading to long thermalization time (see CPGE in the Supplemental Material [5]). In our experiments a superposition of pure right and left circularly polarized light, with relative intensity that can be continuously dialed between the two circular polarization states, shines on the device and the photo-generated current and voltage are simultaneously recorded. The CPGE data is established after careful subtraction of the photothermoelectric (PTE) current, whose behavior is characterized independently.

Our key experimental results are: *i*) A robust finite CPGE is found over a wide range of electron densities and temperatures from ~ 10 K down to 0.3 K, suggesting that the device's point group symmetry is lowered to C_1 at the heterostructure level. *ii*) Low-temperatures PTE voltage data in the same temperature range exhibit features at the integer fillings of $\nu = +1, \pm 2$ and $+3$, as well as at the charge neutrality point (CNP), that become increasingly sharper with lower temperatures, where except for an overall bias that increases with filling, resemble a behavior expected from Mott's semiclassical relation (MSR) [6]. *iii*) An offsetted CPGE sign change near $\nu = 0$ highlights a strong particle-hole asymmetry. While at 1550 nm we might expect the interband effects to dominate, we do observe highly discernible features which are clearly associated with Fermi surface effects as we show in the comparison of the data to the longitudinal electrical resistivity of the device (Fig. 1a). *iv*) Remarkably, at a range of fillings between $\nu = -2.5$ and $\nu = -1.5$, coincidental with the PTE-Voltage deep region around $\nu = -2$, the CPGE vanishes to very high precision. *v*) The zero-CPGE emerges as a sharp onset at $\nu = -1.5$ which remains sharp even at 10 K, suggesting a symmetry breaking effect associated with an energy scale $>$ a few meV. The zero CPGE plateau disappears with a softer, temperature dependent manner below ~ -2.5 .

The above observations correspond more to Fermi-surface tracking of the CPGE, where Berry curvature dipole should dominate, rather than to interband transitions. Indeed, Pantaleón *et al.*, [7] pointed out that a combination of a small uniaxial heterostrain, hexagonal boron nitride (hBN) substrate, and electron-electron interactions treated within a self-consistent Hartree formalism are enough to explain the emergence of strong electron-hole asymmetry and a large Berry Curvature Dipole (BCD) that appears when the chemical potential is tuned to a spectral region entangled with the remote bands. Their calculations largely explained a recent experiment that observed nonlinear Hall currents in MATBG on hBN [8]. In Fig. 1 we show calculation of Berry curvature dipole, where by choosing a reasonable set of device parameters, we find that the band-filling dependence of the CPGE is qualitatively consistent with Berry curvature dipole (BCD) calculations in the presence of strain for negative fillings, while for positive fillings there is a stronger background CPGE that takes the data all positive, yet vestiges of the correlation anomalies can still be observed. While the experimentally measured CPGE vanishes within the interval $-2.5 < \nu < -1.5$, the present Berry-curvature-dipole calculation already produces a very small response in the same filling range, although not an exactly zero signal. The calculation also shows a sign change and a strong inflection centered near $\nu \simeq -2$ for a broad range of effective dipole orientations. This suggests that the observed zero-CPGE plateau is connected to the same Fermi-surface geometric mecha-

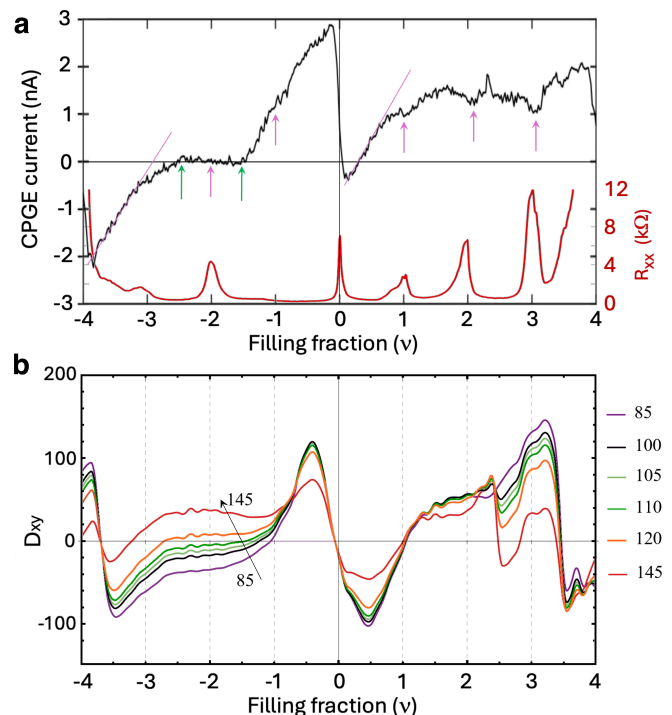


FIG. 1: Top: Measured CPGE current vs. band filling. For comparison we show the longitudinal conductivity that tracks the topological Fermi surface effects. Arrows and straight lines point to the key correlated states in the band. Bottom: Calculation of Berry-Curvature Dipole (BCD) with a uniaxial 0.3 % heterostrain along the K-K' direction. Calculation parameters: Twist-angle, $\theta = 1.05^\circ$, sublattice potential $\Delta_m = 10$ meV, interlayer moire potentials $u = 79.7$ meV and $u' = 97.5$ meV, $\hbar v_F = -2.13a$ with $a = 0.246$ nm, dielectric constant $\epsilon = 6$ and double-gate distance $d_g = 40$ nm. The color legend shows the BCD orientation with respect to the sample.

nism captured by the Berry-curvature dipole calculation. In the experiment, additional correlations not included in the present Hartree treatment may further stabilize this near-zero response and lock the photocurrent to zero (for further discussion on the calculations, see [5]).

RESULTS AND ANALYSIS

We studied a dual-gated MATBG/WSe₂ heterostructure (Fig. 2a). The top gate was fabricated from a thin (3-5 layers) graphite flake to allow optical measurements. Fig. S1 [5] schematically shows our measurement setup. Broadband NIR light (center wavelength- 1550 nm, 3 dB bandwidth, 90 nm) was introduced into a ³He cryostat using a 10 m long polarization maintaining fiber and focused onto a 4.5 μ m spot. A quarter wave-plate (QWP), was oriented such that linearly polarized light aligned

with the fast (slow) axis of the fiber was converted to left (right) circularly polarized light. Normal incidence was guaranteed by maximizing the back-reflected signal that is coupled back into the fiber. The extreme sensitivity of the back-reflected signal to the tip-tilt ensures that the light is normal to within 0.5 deg. A half wave-plate at room temperature was used to rotate the polarization of the light, adjusting the ratio of left/right circularly polarized light incident on the sample. Note that due to the low coherence of the light, the proportion of right and left circularly polarized light was changed without having any intermediate linearly polarized light incident on the sample (Fig. S1). A chopper was used to modulate the intensity of the light, and the photo-current and photo-voltage were measured using lock-in amplifiers. The resistance of the sample was measured separately by biasing the sample with a small ac current (1-10 nA). Photo-resistivity was also measured by removing the chopper and measuring the resistance under illumination. Unless otherwise specified, all data were taken in a zero displacement field, following previous tests that transport properties and optical responses did not show any noticeable displacement field dependence [4].

Fig. 2b shows R_{xx} measured at 300 mK with and without illumination, as a function of filling (in electrons per moire unit cell). As previously reported [4], the transport shows characteristic insulating peaks at integer filling $+1, \pm 2, \pm 3$, which are broadened upon illumination due to light-induced heating, without noticeable photodoping. Given the significant effect of heating on the transport (about 2 K increase in the effective electron temperature), we first characterize the contribution of thermoelectric effects to the photo-transport by measuring photocurrents and photovoltages generated by unpolarized light (Fig. 2d). Measuring simultaneously photovoltage and photocurrent, the deduced Seebeck coefficient also had a smaller contribution from the local resistance. which would only be noticeable at the insulating integer fillings. The measured photovoltages show sharp saw-tooth-like features at charge neutrality, and positive integer fillings, with a more symmetric deep near $\nu = -2$. Indeed, similar features have been observed in near-magic angle bilayer graphene devices with a heater-induced thermoelectric effects [9] or in near-IR unpolarized-light illuminated gate-defined MATBG p-n junctions [10]. Indeed, for unpolarized incident light, polarization-dependent contributions, such as the PGE or geometry-related effects [11–13], should cancel out and we expect the leading contribution to arise from the thermoelectric effect. In fact, the low-temperatures PTE voltage data exhibiting features that become increasingly sharper with lower temperatures, and except for an overall slight bias, it largely resembles a behavior expected

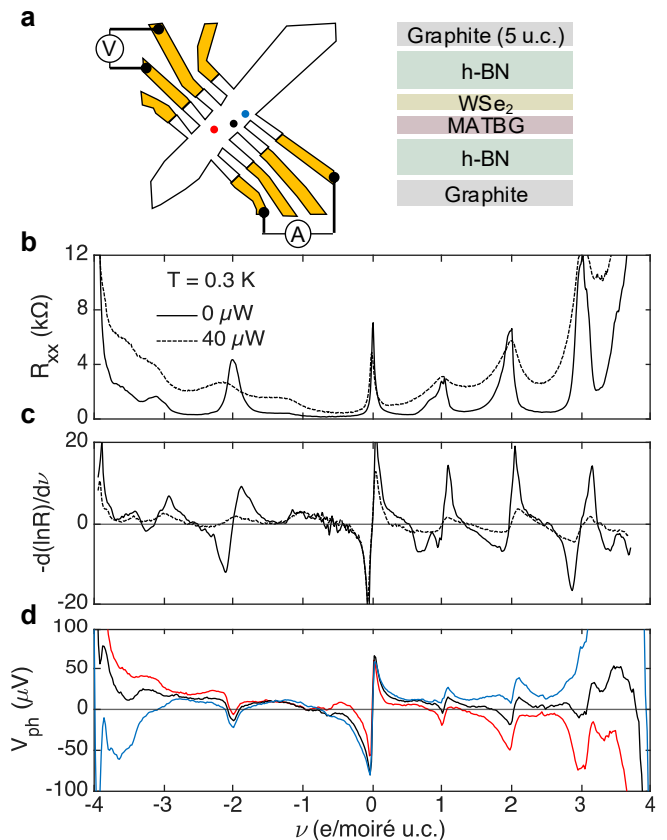


FIG. 2: Schematic of the measurement configuration. For photocurrent measurement, the device is shorted in series with a current amplifier, which measures the current that is induced by the light. The left side shows the van der Waals stack of our dual-gated sample. (b) Longitudinal resistance as a function of carrier density taken at $T = 0.3$ K with and without unpolarized light (incident power, $40 \mu\text{W}$). (c) The photocurrent generated by unpolarized light, compared to the log derivative of the resistance (red curve, proportional to the thermopower).

from Mott’s semiclassical relation [6]:

$$S = -\frac{\pi^2}{3} \frac{k_B^2 T}{e} \frac{\partial \ln \sigma(\mu)}{\partial \mu} \propto \frac{\partial \ln R}{\partial \nu} \frac{\partial \nu}{\partial \mu}, \quad (1)$$

which we show in Fig. 2d. Here k_B is Boltzmann’s constant, T is the temperature, e the electron charge, σ is the conductivity, μ is the chemical potential, R is the resistance and ν is the band filling, proportional to the carrier density. That overall bias was observed near distinct fillings in near magic angle samples [9], and was explained by the interplay between light, long-lived electron states and heavy, short-lived hole excitations near the Fermi level of the symmetry-broken ground states in the MATBG p-n junctions experiments [10].

The total photocurrent collected at the electrodes depends strongly on the geometry of the device and po-

sition of the heat source [14]. Particularly, when the beam is symmetrically positioned between the source and drain electrodes, the distribution of thermal currents is symmetric, and no net current is collected; the thermoelectric currents are maximized when the temperature gradient is localized near the source and drain electrodes. We tested this by raster-scanning the beam over the device, and recording the photocurrent collected at the current-meter as a function of the beam position (Fig. 3a; taken at $T = 4.2$ K and at $\nu = -0.5$), revealing that photocurrent generated by unpolarized light was indeed generated when the beam was positioned over the edge where there is a discontinuity between the thermal conductivity of the MATBG and the leads.

Unlike the thermoelectric current, the CPGE-generated photocurrents have a preferred direction and therefore a distinct spatial signature. To measure the CPGE, we change the polarization of the incident light, and take photocurrent maps for left and right circularly polarized light (CPL). The difference image ΔI_{ph} (Fig. 3c) shows a response that is finite only when the light illuminates the MATBG and does not change sign as the beam is moved from the source to the drain electrode. The observations can be reproduced in simulations assuming the induced current flows along the Hall bar (Fig. 3d). Note that only a part of the MATBG device produces this response. The spatial structure of the polarization dependent response rules out a dichroic contribution, where helicity-dependent absorption leads to stronger thermoelectric effect for right or left CPL. In addition, the concentration of the response at the center of the device rules out contribution from the contacts (which in non-ohmic situations typically induce photovoltaic effects [15–17]), or antenna effects [11] or as the source of the current. We therefore conclude that the measured ΔI_{ph} is a circular photogalvanic current.

We now turn to study the carrier and temperature dependence of the CPGE. Figure 3f shows the photocurrent measured as a function of the carrier density at $T = 4.2$ K. There is a clear difference between the response to right and left CPL at almost all fillings of the moiré unit cell, on top of the thermoelectric contributions which dominate the response. To better visualize the CPGE, we plot the difference between the right and left CPL responses in Fig. 3g. The CPG current changes sign at $\nu = 0$ and $\nu = 1$ and is relatively filling-independent for $1 < \nu < 4$. For hole doping, however, the CPGE vanishes for a wide range of fillings $-2.5 < \nu < -1.5$. At 10 K, which is above the AHE temperature for any filling [3, 4], all the correlated insulator resistive and thermoelectric features are smeared (Fig 3e). However, the CPGE still showed the same overall behavior as in 0.3K, in particular the sharp change in behavior at the neutrality point and the sharp onset of CPGE at $\nu = -1.5$.

DISCUSSION

We first analyze the symmetry requirements for CPGE. We may write the DC photocurrent that is generated by an electric field $\mathbf{E} = \mathbf{E}_0 e^{i\omega t}$ where \mathbf{E}_0 encodes the intensity and polarization of the field, and ω is the frequency as

$$J_i^{(2)} = \zeta_{ijk} (E_j E_k^* + E_k E_j^*) + \eta_{ijk} (E_j E_k^* - E_k E_j^*), \quad (2)$$

where ζ and η encode the linear and circular photogalvanic responses, respectively. Since we measure a 2D sample, the current is in-plane, and normal incidence guarantees $E_z = 0$. Since η is anti-symmetric $\eta_{ijk} = -\eta_{ikj}$, our experiment probes η_{xxy} and η_{yyx} . The normal incidence configuration therefore restricts the symmetry to the non-centrosymmetric gyrotropic groups C_{1h} (alternatively labeled: $\bar{2}$, “m” or C_s), or C_1 (also labeled: 1) [18].

While a single sheet of graphene has D_{6h} point-group symmetry, the symmetry of twisted bilayer graphene is reduced since an incommensurate twist angle reduces the six-fold rotation to three-fold, and breaks inversion. The resulting point group, D_3 , is still too high to support neither AHE states at integer fillings, which we previously reported on it [3, 4], nor CPGE at normal incidence. Further lowering of the symmetry can arise from “structural” origins, such as interaction and alignment to hBN, uniaxial strain, relaxation of atomic positions and twist angle disorder [19], or it may be induced by correlations, such as a nematic state [20] or a charge density wave [21]. The fact that the CPGE does not change qualitatively as a function of filling in the range $1 \leq \nu \leq 4$, and remains present from 0.3 K to 10 K, suggests a structural origin rather than a low-temperature instability. We attribute this low symmetry to the combined effect of asymmetric encapsulation by hBN and WSe₂, together with induced strain, which lowers the effective point group of the device to C_1 . This is consistent with the Berry-curvature-dipole picture discussed below, since in C_1 no point-group symmetry forbids an in-plane Berry-curvature dipole. In addition, the self-consistent Hartree reconstruction modifies the bands on an energy scale of order 10–60 meV, much larger than $k_B T$ in the experimental range, so the corresponding band-geometric response is expected to remain robust from 0.3 K to 10 K.

In this low symmetry, and with our excitation light of 0.8 eV, the remote bands are as important as the flat bands and the most general expression for the circular photogalvanic tensor at normal incidence takes the form:

$$\eta_{ijk}(\omega) = \frac{\pi e^3}{4\hbar^2 \omega} \sum_{n,m} \int \frac{d^2 \mathbf{k}}{(2\pi)^2} f_{nm}(\mathbf{k}) \mathcal{T}_{ijk}^{nm}(\mathbf{k}) \delta(\omega_{mn} - \omega) \quad (3)$$

where ω is the light frequency, n and m are band indices and the generalized injection tensor \mathcal{T}_{ijk}^{nm} includes three

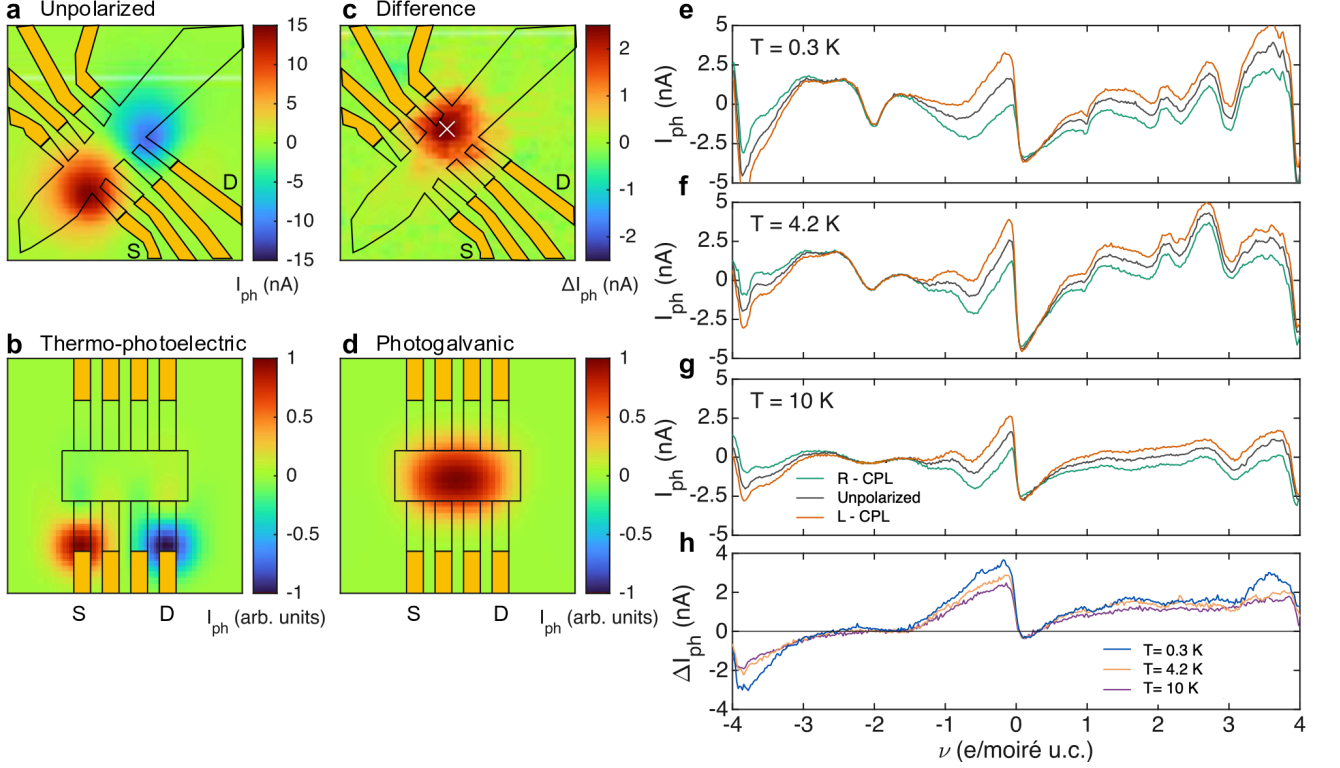


FIG. 3: (a) Experimental photocurrent map taken at filling $\nu = -0.5$ unpolarized light. The device is overlaid on the image based on a simultaneously acquired reflectivity map, and the source and drain electrodes are indicated. (b) Calculated photocurrent map for a Hall bar geometry assuming the photo-induced current originates from local heating through the thermoelectric effect. (c) Difference map of two photocurrent images taken with right- and left-CPL at $\nu = -0.5$. (d) Calculated photocurrent map assuming the photo-induced current originates from a CPGE. (e) Carrier density dependence of the photocurrent for unpolarized and CPL. The beam position is indicated by the cross on panel c. (f) Subtracted curves for right and left CPL from panel e, as well as for similar data at 10 K.

contributions

$$\mathcal{T}_{ijk}^{nm} = \mathcal{T}_{ijk}^{nm,I} + \mathcal{T}_{ijk}^{nm,BC} + \mathcal{T}_{ijk}^{nm,shift} \quad (4)$$

which are in order the I=standard Injection Current due to asymmetric scattering, proportional to the velocity, BC=Berry Curvature Dipole contribution, and shift=shift current, typically associated with the geometric phase. We discuss the details of these terms in the supplemental material ([5]). If scattering is important at least the velocity term will be multiplied by $\tau_{nm}/(1 + \omega^2\tau_{nm}^2)$.

There are primarily two reasons for the moiré quantum geometry effects to appear in the CPGE measurements. First, is when Interband interference between flat band and remote band with different Berry curvatures, which represent a hybrid of interband BCD and shift-current mechanism. Such an interband coherence effect depends on interband dephasing time and various dipole matrix elements, with no explicit dependence on recombination or momentum relaxation. While this effect may dominate the positive fillings, it cannot account for the close correspondence between the calculation and the experiment for negative fillings. The second mechanism assumes that

the photoexcited carriers cascade into the flat band and then respond via anomalous velocity, which we call a pumped BCD mechanism. Here 0.8 eV photons excite carriers from occupied bands into remote (graphene-like continuum) bands via interband transitions $n \rightarrow m$ with $\hbar\omega_{mn} \sim 0.8$ eV. These hot carriers rapidly relax/cascade down through phonon and e-e scattering within a time-scale much faster than either momentum relaxation or recombination times, eventually accumulating in the flat band (which lies near the Fermi level). Once in the flat band, the (now long-lived) photoexcited distribution $\delta f_{F\mathbf{k}}^{(A)}$ and experiences an anomalous (Berry-curvature) velocity:

$$\mathbf{v}_{an} = -\frac{e}{\hbar} \mathbf{E}(t) \times \Omega_F^z(\mathbf{k}) \hat{z}, \quad (5)$$

under the driving optical field $\mathbf{E}(t)$. The product of the helicity-odd $\delta f^{(A)}$ and the Berry-curvature anomalous velocity yields a DC current proportional to Ω_F^z , or its dipole $\partial_k \Omega_F^z$

$$D_{\text{pumped}}^{zl}(\omega) = \sum_n \int \frac{d^2\mathbf{k}}{(2\pi)^2} \partial_{k_l} \Omega_n^z(\mathbf{k}) [\delta f_{n\mathbf{k}}^{(A)}(\omega)] \quad (6)$$

which is the same expression as for the equilibrium Berry curvature sampled near the chemical potential, except for $f_{n\mathbf{k}} \rightarrow \delta f_{F\mathbf{k}}^{(A)}$.

The persistence of the CPGE response to above 10 K may also suggest that a Hartree approach, where coulomb interactions are considered at the mean-field level, but the effect of the encapsulation and strain are considered may capture the essence of the observed CPGE through the calculation of the Berry curvature dipole. Indeed, as emphasized at the outset of this paper, there is a remarkable qualitative agreement between such calculations and the observed CPGE, except in the range $-2.5 \leq \nu \leq -1.5$, where the CPGE vanishes to a very high degree. We note however that the Berry-Curvature Dipole calculations do find a sign change centered around $\nu = -2$ with a wide plateau region may indicate that the observed zero-plateau emerges from the same effect, possibly in the presence of strong correlations not included in the present model which pin the plateau at zero (for further discussion on the calculations, see [5]).

While the Seebeck coefficient, similar to the longitudinal conductivity, does not involve quantum geometry effects within straightforward semiclassical Boltzmann-Mott approach, we already noted above that the overall bias in the photovoltage, which shifts away the sign change at integer fillings expected from SMR points to a non-Fermi-liquid behavior in that temperature regime (Fig. 2d). nevertheless, we do observe that as we lower the temperature towards base temperature, the sawtooth-like response of the PTE response gets sharper and exhibiting a weaker bias, which we interpret as moving towards a Fermi liquid behavior at lower temperatures. At the same time, a Hartree approach with the same fit parameters used to calculate the BCD fails to reproduce the photovoltage results at any temperature (see Supplemental Materials [5]).

The observations above indicate that the Hartree-renormalized Berry-curvature-dipole picture captures the tendency toward a suppressed CPGE near $\nu \simeq -2$, but does not by itself explain either the detailed PTE response or the exact vanishing of the CPGE over a finite filling interval. These features suggest that additional correlation effects, possibly involving a reconstructed electronic state, are relevant. Indeed, correlations at least at the exchange level have been essential to explain the correlated Chern insulator (CCI) states in MATBG, with Chern numbers $|t| = 1, 2, 3$ and moiré filling factors $|s| = 3, 2, 1$ [22–27]. For the same MATBG device studied here, He et al. [3] reported a detailed study of CCI states, together with a cascade of symmetry-broken Chern insulator (SBCI) states that appear primarily upon hole doping of the magnetic subbands. These SBCI states were proposed to retain the spin and valley polarization properties of a parent CCI, while further breaking moiré translation symmetry through a charge-density wave that doubles the moiré unit-cell area [3].

In particular, Ref. [3] showed that the SBCI $(-2, -3/2)$ state, which is relevant to the filling range discussed here, terminates at a threshold magnetic field near a distinct state identified as a gapped incommensurate Kekulé spiral (IKS). The two states meet at the rational flux ratio $\Phi/\Phi_0 = 1/4$ [3]. In the present experiment, however, the sharp onset of the zero-CPGE regime occurs near $\nu = -1.5$ already at zero magnetic field. This suggests, as a reasonable conjecture, that the zero-field state may be related to the same tendency toward moiré unit-cell doubling inferred from the high-field SBCI $(-2, -3/2)$ state. Since the zero-CPGE region is centered near $\nu = -2$, this conjecture is also naturally connected to the van Hove singularity, where the Fermi level is susceptible to pinning and the charge distribution is especially sensitive to the self-consistent electrostatic potential. STM studies of MATBG on hBN have reported a $\sqrt{3} \times \sqrt{3}$ reconstruction at the graphene atomic scale near the correlated insulator at $\nu = -2$ [28]. They also found broken translation and rotational symmetries on the moiré scale, with stripe-like features.

As argued above, the hBN substrate, the WSe₂ cap, and the induced strain reduce the structural symmetry of the device to C₁. In this low-symmetry environment, a unidirectional 1Q stripe CDW with a preferred moiré *M* direction is a natural translation-symmetry-breaking instability. Such a state could double the moiré unit cell near $\nu = -1.5$, providing a possible zero-field counterpart of the high-field SBCI $(-2, -3/2)$ state. A related theoretical precedent was recently found in strained graphene superlattices, where enlarged-unit-cell calculations showed that a purely self-consistent Hartree potential can stabilize translation-symmetry-broken charge configurations, without requiring a magnetic field or exchange-driven order [29].

While the above discussion focuses on electronic structure near the Fermi level, the optical excitation energy in our experiment is $\hbar\omega \simeq 0.8$ eV. At this energy, the CPGE is likely to receive substantial contributions from inter-band injection processes involving remote moiré bands, including higher conduction bands, deeper valence bands, and states with appreciable weight in the graphene-like Dirac sectors. Therefore, the exact cancellation of the CPGE should not be interpreted as a purely low-energy flat-band effect. Rather, the unit-cell-doubling scenario should be viewed as a possible additional ingredient to the Berry-curvature-dipole picture discussed above. The Berry-curvature-dipole calculation already produces a nearly vanishing response near $\nu \simeq -2$, suggesting that the dominant tendency toward suppression is associated with the Hartree-renormalized band geometry near the van Hove singularity. A translation-symmetry-broken state could further reconstruct the bands by folding states at \mathbf{k} and $\mathbf{k} + \mathbf{Q}$, redistributing optical transitions among the folded eigenstates and allowing a stronger cancellation of helicity-dependent contributions. A more rig-

orous account of this possible reconstructed state and of its full-band optical response in the present MATBG device requires further theoretical development and is left for future work.

In conclusion, we observed a strong CPGE signal, which indicates that the symmetry of MATBG capped with WSe₂ and encapsulated with hBN is as low as C₁. This low symmetry gives rise to strong optical effects, with an unusual surprise of a vanishing CPGE around $\nu = -2$ filling. While sign change around this filling is observed in Berry curvature dipole, a range of filling with zero CPGE indicates an effective increase in symmetry, which we propose is connected to a moiré unit cell doubling. Obviously a more complete theory, which presumably should include correlations at the full band structure level is needed to explain this data.

ACKNOWLEDGMENTS

We thank Andrei Bernevig and Steve Kivelson for fruitful discussions. Work at Stanford University was supported by the U. S. Department of Energy (DOE) Office of Basic Energy Science, Division of Materials Science and Engineering at Stanford under contract No. DE-AC02-76SF00515. EP was partially supported by the Koret Foundation. Work at the University of Washington is supported by NSF MRSEC DMR-1719797.

DATA AVAILABILITY

The data that support the findings of this study are available from the corresponding authors upon reasonable request.

* perskye1@stanford.edu

- [1] Y. Cao, V. Fatemi, A. Demir, S. Fang, S. L. Tomarken, J. Y. Luo, J. D. Sanchez-Yamagishi, K. Watanabe, T. Taniguchi, E. Kaxiras, *et al.*, Correlated insulator behaviour at half-filling in magic-angle graphene superlattices, *Nature* **556**, 80 (2018).
- [2] Y. Cao, V. Fatemi, S. Fang, K. Watanabe, T. Taniguchi, E. Kaxiras, and P. Jarillo-Herrero, Unconventional superconductivity in magic-angle graphene superlattices, *Nature* **556**, 43 (2018).
- [3] M. He, X. Wang, J. Cai, J. Herzog-Arbeitman, R. Peng, T. Taniguchi, K. Watanabe, A. Stern, B. A. Bernevig, M. Yankowitz, O. Vafek, and X. Xu, Strongly interacting hofstadter states in magic-angle twisted bilayer graphene, *Nature Physics* **21**, 1380–1386 (2025).
- [4] E. Persky, L. Parisot, M. He, J. Cai, T. Taniguchi, K. Watanabe, J. May-Mann, X. Xu, and A. Kapitulnik, Optical control of orbital magnetism in magic-angle twisted bilayer graphene, *Nature Physics* **22**, 39–46 (2026).
- [5] this paper, Supplemental information (2026), url to be determined by publisher.
- [6] M. Cutler and N. F. Mott, Observation of anderson localization in an electron gas, *Phys. Rev.* **181**, 1336 (1969).
- [7] P. A. Pantaleón, V. o. T. Phong, G. G. Naumis, and F. Guinea, Interaction-enhanced topological hall effects in strained twisted bilayer graphene, *Phys. Rev. B* **106**, L161101 (2022).
- [8] J. Duan, Y. Jian, Y. Gao, H. Peng, J. Zhong, Q. Feng, J. Mao, and Y. Yao, Giant second-order nonlinear hall effect in twisted bilayer graphene, *Phys. Rev. Lett.* **129**, 186801 (2022).
- [9] B. Ghawri, P. S. Mahapatra, M. Garg, S. Mandal, S. Bhowmik, A. Jayaraman, R. Soni, K. Watanabe, T. Taniguchi, H. R. Krishnamurthy, M. Jain, S. Banerjee, U. Chandni, and A. Ghosh, Breakdown of semiclassical description of thermoelectricity in near-magic angle twisted bilayer graphene, *Nature Communications* **13**, 1522 (2022).
- [10] R. L. Merino, D. Călugăru, H. Hu, J. Díez-Mérida, A. Díez-Carlón, T. Taniguchi, K. Watanabe, P. Seifert, B. A. Bernevig, and D. K. Efetov, Interplay between light and heavy electron bands in magic-angle twisted bilayer graphene, *Nature Physics*, 1 (2025).
- [11] S. Castilla, B. Terrés, M. Autore, L. Viti, J. Li, A. Y. Nikitin, I. Vangelidis, K. Watanabe, T. Taniguchi, E. Lidorikis, *et al.*, Fast and sensitive terahertz detection using an antenna-integrated graphene pn junction, *Nano letters* **19**, 2765 (2019).
- [12] S. Candussio, M. Durnev, S. Tarasenko, J. Yin, J. Keil, Y. Yang, S.-K. Son, A. Mishchenko, H. Plank, V. Bel'kov, *et al.*, Edge photocurrent driven by terahertz electric field in bilayer graphene, *Physical Review B* **102**, 045406 (2020).
- [13] V. A. Semkin, A. V. Shabanov, D. A. Mylnikov, M. A. Kashchenko, I. K. Domaratskiy, S. S. Zhukov, and D. A. Svintsov, Zero-bias photodetection in 2d materials via geometric design of contacts, *Nano Letters* **23**, 5250 (2023).
- [14] J. C. W. Song and L. S. Levitov, Shockley-ramo theorem and long-range photocurrent response in gapless materials, *Phys. Rev. B* **90**, 075415 (2014).
- [15] E. J. H. Lee, K. Balasubramanian, R. T. Weitz, M. Burghard, and K. Kern, Contact and edge effects in graphene devices, *Nature Nanotechnology* **3**, 486 (2008).
- [16] J. Park, Y. H. Ahn, and C. Ruiz-Vargas, Imaging of photocurrent generation and collection in single-layer graphene, *Nano Letters* **9**, 1742 (2009).
- [17] F. Xia, T. Mueller, Y.-m. Lin, A. Valdes-Garcia, and P. Avouris, Ultrafast graphene photodetector, *Nature Nanotechnology* **4**, 839 (2009).
- [18] R. R. Birss, Macroscopic symmetry in space-time, *Reports on Progress in Physics* **26**, 307 (1963).
- [19] A. Uri, S. Grover, Y. Cao, J. A. Crosse, K. Bagani, D. Rodan-Legrain, Y. Myasoedov, K. Watanabe, T. Taniguchi, P. Moon, M. Koshino, P. Jarillo-Herrero, and E. Zeldov, Mapping the twist-angle disorder and landau levels in magic-angle graphene, *Nature* **581**, 47–52 (2020).

- [20] Y. Cao, D. Rodan-Legrain, J. M. Park, N. F. Q. Yuan, K. Watanabe, T. Taniguchi, R. M. Fernandes, L. Fu, and P. Jarillo-Herrero, Nematicity and competing orders in superconducting magic-angle graphene, *Science* **372**, 264–271 (2021).
- [21] Y. Jiang, X. Lai, K. Watanabe, T. Taniguchi, K. Haule, J. Mao, and E. Y. Andrei, Charge order and broken rotational symmetry in magic-angle twisted bilayer graphene, *Nature* **573**, 91–95 (2019).
- [22] K. P. Nuckolls, M. Oh, D. Wong, B. Lian, K. Watanabe, T. Taniguchi, B. A. Bernevig, and A. Yazdani, Strongly correlated chern insulators in magic-angle twisted bilayer graphene, *Nature* **588**, 610 (2020).
- [23] Y. Saito, J. Ge, L. Rademaker, K. Watanabe, T. Taniguchi, D. A. Abanin, and A. F. Young, Hofstadter subband ferromagnetism and symmetry-broken chern insulators in twisted bilayer graphene, *Nature Physics* **17**, 478 (2021).
- [24] J. M. Park, Y. Cao, K. Watanabe, T. Taniguchi, and P. Jarillo-Herrero, Flavour hund’s coupling, chern gaps and charge diffusivity in moiré graphene, *Nature* **592**, 43 (2021).
- [25] Y. Choi, H. Kim, Y. Peng, A. Thomson, C. Lewandowski, R. Polski, Y. Zhang, H. S. Arora, K. Watanabe, T. Taniguchi, J. Alicea, and S. Nadj-Perge, Correlation-driven topological phases in magic-angle twisted bilayer graphene, *Nature* **589**, 536 (2021).
- [26] I. Das, X. Lu, J. Herzog-Arbeitman, Z.-D. Song, K. Watanabe, T. Taniguchi, B. A. Bernevig, and D. K. Efetov, Symmetry-broken chern insulators and rashba-like landau-level crossings in magic-angle bilayer graphene, *Nature Physics* **17**, 710 (2021).
- [27] S. Wu, Z. Zhang, K. Watanabe, T. Taniguchi, and E. Y. Andrei, Chern insulators, van hove singularities and topological flat bands in magic-angle twisted bilayer graphene, *Nature Materials* **20**, 488 (2021).
- [28] K. P. Nuckolls, R. L. Lee, M. Oh, D. Wong, T. Soejima, J. P. Hong, D. Călugăru, J. Herzog-Arbeitman, B. A. Bernevig, K. Watanabe, T. Taniguchi, N. Regnault, M. P. Zaletel, and A. Yazdani, Quantum textures of the many-body wavefunctions in magic-angle graphene, *Nature* **620**, 525 (2023).
- [29] E. Andrade, A. Jimeno-Pozo, P. A. Pantaleon, F. Guinea, and G. G. Naumis, Electrostatic charge fractionalization and unconventional superconductivity in strained monolayer graphene (2025), arXiv:2507.00112.

SUPPLEMENTAL MATERIAL

Revealing structural chirality in magic angle twisted bilayer graphene using the photogalvanic effect

Eylon Persky,^{1,2,3*} Léonie Parisot,¹ Minhao He,⁴ Jiaqi Cai,⁴ Takashi Taniguchi,⁵ Kenji Watanabe,⁶ Pierre A. Pantaleón,⁷
Francisco Guinea,^{7,8} Xiaodong Xu,⁴ and Aharon Kapitulnik^{1,2,3,9}

¹*Geballe Laboratory for Advanced Materials, Stanford University, Stanford, California 94305, USA*

²*Stanford Institute for Materials and Energy Sciences, SLAC National Accelerator Laboratory, 2575 Sand Hill Road, Menlo Park, California 94025, USA*

³*Department of Applied Physics, Stanford University, Stanford, California 94305, USA*

⁴*Department of Physics, University of Washington, Seattle, Washington, 98195, USA*

⁵*Research Center for Materials Nanoarchitectonics, National Institute for Materials Science, 1-1 Namiki, Tsukuba 305-0044, Japan.*

⁶*Research Center for Electronic and Optical Materials, National Institute for Materials Science, 1-1 Namiki, Tsukuba 305-0044, Japan*

⁷*Imdea Nanoscience, Faraday 9, 28047 Madrid, Spain* ⁸*Donostia International Physics Center, Paseo Manuel de Lardizábal 4, 20018 San Sebastián, Spain* ⁹*Department of Physics, Stanford University, Stanford, California 94305, USA*

METHODS

Device fabrication

The hetero-structure was assembled using a standard dry-transfer technique with a PC/PDMS (polycarbonate/polydimethylsiloxane) stamp, and transferred onto a Si/SiO₂ wafer. The twisted bilayer graphene was fabricated by using the tear-and-stack method. The top gate was a 3-5 layer thick graphene flake, in order to minimize its optical absorption. The back graphite gate was 3-5 nm thick. The Hall bar geometry was defined using CHF₃/O₂ and O₂ plasma etching, followed by electron beam lithography. Cr/Au contacts (7nm/70nm) were added using electron beam evaporation.

Thermoelectric Effects

Experimental Considerations

The Seebeck effect occurs when a temperature difference between two points in an electrically conducting material generates an electromotive force (EMF). The resulting current density is

$$\mathbf{j} = \sigma(-\nabla V + \mathbf{E}_{\text{emf}}) \quad \text{where} \quad \mathbf{E}_{\text{emf}} = -S\nabla T \quad (\text{S.1})$$

In a typical experiment no current is withdrawn while the voltage generated by the temperature gradient is measured and $S = -\Delta V/\Delta T$. However, in our experiment we measured simultaneously the thermoelectric voltage and the induced current. In such a measurement, with the assumption of a perfect current meter, the measured voltage due to the temperature gradient is

$$\Delta V_{\text{measured}} = -S\Delta T + \frac{1}{3}\Delta I_{\text{measured}}\Delta R \quad (\text{S.2})$$

where R is the resistance and the division by 3 stems from the ratio of distances between the voltage and current leads (see Fig. 2a in the main text). We can estimate that in the metallic regimes between the correlated insulator peaks the finite current yields a correction $\lesssim 1 \mu\text{V}$, while at the resistance peaks at $\nu = -3, -2, 0, +1, +2, +3$ the correction is at most $10 \mu\text{V}$. Comparing these estimates to the thermoelectric photovoltage in Fig. 2d, the thermoelectric photocurrent may introduce at most a 10% error in the calculated Seebeck coefficient.

Guideline Theory

The electronic properties of MATBG are determined by the flat bands and strong correlations, especially near integer fillings. Let's take the simplest approach where at integer fillings there is a gap, while in between we have a metallic state dominated by diffusive scattering. A simple phenomenological model for the Seebeck coefficient will be

$$S_{\text{tot}}(\nu, T) = S_{\text{met}}(\nu, T) + S_{\text{gap}}(\nu, T) \quad (\text{S.3})$$

Here $S_{\text{met}}(\nu, T)$ accounts for the variation of the band structure's density of states as a function of filling excluding the correlated insulating states, and $S_{\text{gap}}(\nu, T)$ is the Seebeck coefficient of a gapped insulator with a gap $\Delta(T)$. The simplest approach for a gapped Seebeck coefficient is to say that activated carriers carry energy $\sim \Delta$, so thermovoltage per temperature-K is $\sim \Delta/(eT)$. This gives an estimate:

$$S_{\text{gap}}(\nu, T) \sim \pm \frac{k_B}{e} \frac{\Delta}{k_B T} \quad (\text{S.4})$$

where the sign depends if the activated carriers are electrons or holes.

The in-between integer fillings will be dominated by the band structure DOS. Here we can use the Mott's formula

$$S(\nu, T) \approx S_{\text{met}}(\nu, T) = -\frac{\pi^2 k_B^2 T}{3e} \left. \frac{d \ln \sigma(\epsilon)}{d\epsilon} \right|_{\epsilon=\epsilon_F(\nu)} \quad (\text{S.5})$$

In these in between metallic regime $S(\nu, T) \propto T$ is expected to be small at low temperatures.

The main issue is how to include a possible energy-dependent scattering rate, which influences the conductivity at the same time as the density of states. Here we propose that in a similar way to treating the optical conductivity of correlated metals, where an Extended Drude Model is used such that instead of treating the scattering rate $1/\tau$ and mass m^* as constants, they become frequency dependent. This is then parametrized through a fractional power law: $\sigma_1(\omega) \propto \omega^{-\alpha}$ rather than the standard Drude decay $\sigma_1(\omega) \propto \omega^{-2}$ and typically $\alpha < 2$. In the same spirit, we can assume that the conductivity that goes into the Mott's formula has the following energy dependence: $\sigma(\epsilon) \propto \epsilon^\alpha$, which yields the approximate Seebeck coefficient:

$$S_{\text{met}}(\nu, T) \approx -\frac{\pi^2 k_B^2 T}{3e} \frac{\alpha}{\epsilon_F^*(\nu)} \quad (\text{S.6})$$

With this expression, we see that $S(\nu)$ depends on the sign (electron vs hole), the inverse renormalized Fermi energy $1/\epsilon_F^*(\nu)$, and changes in an effective exponent α near band-structure important features such as van Hove singularities. This predicts largest thermopower for small ϵ_F^* , often expected near the incompressible fillings. The bottom line is we need to find $\epsilon_F^*(\nu)$ to calculate $S_{\text{met}}(\nu, T)$.

To compare with our CPGE results, If Hartree is the main filling-dependent effect and correlations are weak (excluding the sharp features at integer fillings), we may expect broad features associated with the van-Hove singularities (vHs).

CPGE

General Considerations

$$j_i = \eta_{ijl}(\omega)(E_j E_l^* - E_l E_j^*) \equiv \eta_{ijl}(\omega) \Xi_{jl}, \quad \text{where} \quad \Xi_{jl} = -\Xi_{lj}. \quad (\text{S.7})$$

For circular polarization with $\mathbf{E} = E_0(\hat{x} \pm i\hat{y})$ and at normal incidence light propagates along z . The general form for η_{ijl} is:

$$\eta_{ijl}(\omega) = \frac{\pi e^3}{4\hbar^2 \omega} \sum_{n,m} \int \frac{d^2 \mathbf{k}}{(2\pi)^2} f_{nm}(\mathbf{k}) \mathcal{T}_{ijl}^{nm}(\mathbf{k}) \delta(\omega_{mn}(\mathbf{k}) - \omega) \quad (\text{S.8})$$

where in general we include lifetime broadening through the replacement:

$$\delta(\omega_{mn} - \omega) \longrightarrow \delta_{\Gamma}(\omega_{mn} - \omega) \equiv \frac{1}{\pi} \frac{\Gamma}{(\omega_{mn} - \omega)^2 + \Gamma^2} \quad (\text{S.9})$$

Within this formulation the injection tensor contains three contributions:

$$\mathcal{T}_{ijl}^{nm} = \mathcal{T}_{ijl}^{nm,\text{I}} + \mathcal{T}_{ijl}^{nm,\text{shift}} + \mathcal{T}_{ijl}^{nm,\text{BC}} \quad (\text{S.10})$$

where the Standard Injection Current (Asymmetric Scattering) is:

$$\mathcal{T}_{ijl}^{nm,\text{I}} = 2 \text{Im}[r_{nm}^j r_{mn}^l] v_{mn}^i \quad (\text{S.11})$$

where $v_{mn}^i = \frac{1}{\hbar} \partial_{k_i} (E_m - E_n) = v_m^i - v_n^i$ is the velocity difference and $r_{nm}^i = \langle n | i \partial_{k_i} | m \rangle$ is the interband position matrix element. The Shift Current (Geometric Phase) is then given by:

$$\mathcal{T}_{ijl}^{nm,\text{shift}} = 2 \text{Im}[r_{nm}^j r_{mn}^l] R_{nm}^i \quad (\text{S.12})$$

where the shift vector is: $R_{nm}^i(\mathbf{k}) = i \sum_{p \neq n, m} \left(\frac{r_{np}^i r_{pm}^l}{\omega_{pn}} - \frac{r_{np}^l r_{pm}^i}{\omega_{pm}} \right) + \partial_{k_i} \arg[r_{nm}^l]$.

Berry Curvature Effects

In a standard approach we would expect that in equilibrium we could distinguish interband from intraband effects:

$$\mathcal{T}_{ijl}^{nm,\text{BC}}(\omega) = \mathcal{T}_{ijl}^{nm,\text{BC-inter}} + \mathcal{T}_{ijl}^{nn,\text{BC-intra}} \quad (\text{S.13})$$

with

$$\mathcal{T}_{ijl}^{nm,\text{BC-inter}} = 2 \text{Im}[r_{nm}^j r_{mn}^l] \Delta \Omega_{nm}^i \quad (\text{S.14})$$

where $\Delta \Omega_{nm}^i = \Omega_m^i(\mathbf{k}) - \Omega_n^i(\mathbf{k})$ is the Berry curvature difference between bands m and n . and

$$\mathcal{T}_{ijl}^{nn,\text{BC-intra}} = 2 \text{Im}[r_{nm}^j r_{mn}^l] \Delta \Omega_{nm}^i \quad (\text{S.15})$$

As for the intraband contribution, reverting to η_{ijl} , we expect a direct dependence on the Berry curvature dipole tensor:

$$\eta_{ijl}^{\text{BC-intra}}(\omega) = \frac{e^3 \tau}{2\hbar^2} \frac{1}{1 + \omega^2 \tau^2} \left(\epsilon_{ijp} D_{pl} - \epsilon_{ilp} D_{pj} \right) \quad (\text{S.16})$$

where ϵ_{ijp} is the totally antisymmetric Levi-Civita tensor, and D_{pl} is the intraband Berry curvature dipole given by:

$$D_{pl} = \sum_n \int \frac{d^2 k}{(2\pi)^2} f_{n\mathbf{k}} \partial_{k_l} \Omega_n^m(\mathbf{k}) = - \sum_n \int \frac{d^2 k}{(2\pi)^2} (\partial_{k_l} f_{n\mathbf{k}}) \Omega_n^m(\mathbf{k}) \quad (\text{S.17})$$

Note that in strictly 2D only Ω_n^z is nonzero and thus only D_{zl} is relevant. Obviously, for high frequencies such as our excitation light at $\hbar\omega \approx 0.8$ eV, we expect $\omega\tau \gg 1$ and therefore a strong reduction in capturing this effect.

Berry Curvature Dipole from Optical Pumping

However, based on the remarkable correspondence between our CPGE data and calculations that focus on the Fermi-surface using eqn. S.17, we note that the above intraband approach can also emerge through an optical pumping process, where the high-energy photon excites carriers via interband transitions $n \leftrightarrow m$, which in turn creates a nonequilibrium $\delta f_n(\mathbf{k}; \omega)$ or $\delta f_m(\mathbf{k}; \omega)$. Since our aim is to focus on pure CPGE at normal incidence, we use the superscript (A) to select only the helicity-odd optical pumping kernel and focus on 2D

$$\mathcal{W}_{nm,jl}^{(A)}(\mathbf{k}; \omega) = \frac{2\pi e^2}{\hbar^2} \text{Im}[r_{nm}^j r_{mn}^l] \delta_{\Gamma}(\omega_{mn} - \omega) \quad (\text{S.18})$$

The respective helicity-odd change in distribution function is:

$$\delta f_{n\mathbf{k}}^{(A)}(\omega) = \tau_n^{\text{rec}} \sum_{m \neq n} f_{nm}(\mathbf{k}) \mathcal{W}_{nm,jl}^{(A)}(\mathbf{k}; \omega) \Xi_{jl} \quad (\text{S.19})$$

where $f_{nm} = f_n - f_m$ and τ_n^{rec} is a phenomenological population relaxation/recombination time for the photoexcited distribution (can differ strongly from momentum relaxation time). The anomalous velocity in band n resulting from a monochromatic electric field $E_j(t) = \text{Re}\{E_j e^{-i\omega t}\}$ is:

$$\tilde{v}_n^i(\mathbf{k}, t) = -\frac{e}{\hbar} \epsilon_{ijl} E_j(t) \Omega_n^l(\mathbf{k}) \quad (\text{S.20})$$

which in turn give rise to a ‘‘pumped Berry curvature current’’ given by (in 2D):

$$j_i^{(\text{BC, pumped})}(\omega) = -\frac{e^2}{\hbar} \sum_n \int \frac{d^2\mathbf{k}}{(2\pi)^2} \epsilon_{ijz} \Omega_n^z(\mathbf{k}) \mathcal{D}_n(\omega) \left[\delta f_{n\mathbf{k}}^{(A)}(\omega) \right] E_j \quad (\text{S.21})$$

where we added a Drude frequency factor $\mathcal{D}_n(\omega) = 1/(1 + i\omega\tau)$.

In a similar fashion that we obtained the Berry curvature dipole in the equilibrium case, here to obtain the ‘‘pumped Berry curvature dipole’’ we need to expand the current to the next order derivative of the nonequilibrium distribution.

$$D_{\text{pumped}}^{zl}(\omega) \equiv \sum_n \int \frac{d^2\mathbf{k}}{(2\pi)^2} \partial_{k_l} \Omega_n^z(\mathbf{k}) \delta f_{n\mathbf{k}}^{(A)}(\omega) \quad (\text{S.22})$$

Substituting $\delta f^{(A)}$ we obtain the final result:

$$D_{\text{pumped}}^{zl}(\omega) = \sum_n \tau_n^{\text{rec}} \int \frac{d^2\mathbf{k}}{(2\pi)^2} \partial_{k_l} \Omega_n^z(\mathbf{k}) \sum_{m \neq n} f_{nm}(\mathbf{k}) \mathcal{W}_{nm,jl}^{(A)}(\mathbf{k}; \omega) \Xi_{xy} \quad (\text{S.23})$$

The ‘‘pumped’’ BCD and application of optically-pumped BCD in MATBG

In the manuscript we argue that the Berry curvature dipole that gives rise to the CPGE current in our experiments seems to follow the equilibrium BCD at the Fermi surface, which is dominated by the flat band. Therefore, we first ask the question of what are the conditions that the flat band dominates the behavior, at least in a proportionality fashion.

For this to happen, we first require that the thermalization time scale, τ_{th} is much shorter compared to either momentum relaxation or recombination time, so that the band reaches a quasi-Fermi distribution. That is, after a fast cascade into the flat bands and rapid intraband thermalization $\delta f^{(A)}$ can become quasi-thermal, which means that D_{pumped} can become $\propto D_{\text{eq}}$ (where the subscript ‘‘eq’’ stands for the equilibrium BCD). In particular, we require that light doesn’t activate a new symmetry channel that equilibrium doesn’t have. Within such conditions $\delta f_{n\mathbf{k}}^{(A)}$ is practically a correction to the equilibrium distribution function in the flat band. Focusing on the flat band, with its equilibrium distribution $f_F^{(0)}$, we can write

$$\delta f_{F\mathbf{k}} \approx -\frac{\partial f_F^{(0)}}{\partial \epsilon} \delta \mu - \frac{\partial f_F^{(0)}}{\partial T} \delta T, \quad (\text{S.24})$$

and in thermal equilibrium, only the chemical-potential shift piece survives, giving exactly the equilibrium BCD weighting

$$D_{\text{pumped}}^{zl} \approx \delta \mu \int_{\mathbf{k}} \left(-\frac{\partial f_F^{(0)}}{\partial \epsilon} \right) \partial_{k_l} \Omega^z = \delta \mu D_{\text{eq}}^{zl} \quad (\text{S.25})$$

Note also that we also assume that during the illumination process the Berry curvature landscape is the equilibrium one: $\Omega_f^z(\mathbf{k})$ (during illumination) $\approx \Omega_{f,\text{eq}}^z(\mathbf{k})$. This is justified in our experiments where we demonstrated no discernible photodoping effects with the light intensity we used

Other routes to obtaining BCD that is roughly proportional to the equilibrium flat band one involves a pumping kernel that is almost \mathbf{k} -independent. However, at $\hbar\omega \sim 0.8$ eV in MATBG, resonant transitions usually involve remote bands with sizable dispersion; without strong broadening/relaxation, the pumping is typically quite \mathbf{k} -selective.

With the above assumptions, we indeed expect that

$$D_{\text{pumped}}^{zl}(\omega) \approx C(\omega) D_{\text{eq}}^{zl} \quad (\text{S.26})$$

where $C(\omega)$ is a proportionality factor that depends on the light frequency.

Transport and photocurrent measurements

The measurements were conducted in a Janis ^3He cryostat. For transport measurements, an a.c. current (1-5 nA rms, frequency 11 Hz) was applied to the sample, and the resulting voltage was read using a lock-in amplifier. To tune the carrier density and displacement fields, top and bottom gate voltages were applied using two Keithley 2450 units, according to $n = C_T(V_{TG} - V_{TG}^0) + C_B(V_{BG} - V_{BG}^0)$ and $D = [C_T(V_{TG} - V_{TG}^0) - C_B(V_{BG} - V_{BG}^0)]/2\epsilon_0$, where C_T (C_B) is the capacitance per unit area of the top (bottom) gate. For the photo-current measurement, one electrical contact to the MATBG was grounded and a second contact was connected in series with a trans-impedance amplifier (Keithley 427) and then to ground. A second pair of contacts was connected to a voltage preamplifier (SR560, input impedance 100 M Ω) for simultaneous measurement of the photo-voltage. The rest of the contacts were floating. Lock-in amplifiers were then used to isolate the response at the chopper frequency.

Optical setup

Light from a low-coherence source (superluminescent diode, DenseLight DL-CS5169A) was introduced into the cryostat via a 10 m-long single-mode polarization maintaining fiber (Thorlabs PM-1550XP). A pair of aspheric lenses was used to collimate and re-focus the light, resulting in a gaussian intensity profile incident on the sample, with a spot size that is determined by the ratio of the two focal lengths. In this study, a spot size of 4.5 μm was selected to match the dimensions of the device. A zero-order quarter wave-plate (Thorlabs WQP501) was aligned at 45 $^\circ$ with respect to the fast axis of the fiber, in order to convert light linearly polarized along the slow/fast axis to right/left circular polarization.

The lens tube was mounted on a piezo-based xy scanner to allow accurate positioning of the beam over the device at low temperatures. A piezo-based stick-slip positioner (Attocube ANPz101) was used to bring the sample into the focal plane of the lens. Finally, a manually-adjustable tip-tilt stage was used at room temperature to align the beam at normal incidence to the sample. At cryogenic temperatures, the lens tube was scanned over the device and the image of the reflected light intensity was compared to the optical microscope image of the device in order to then position the beam over the hetero-structure.

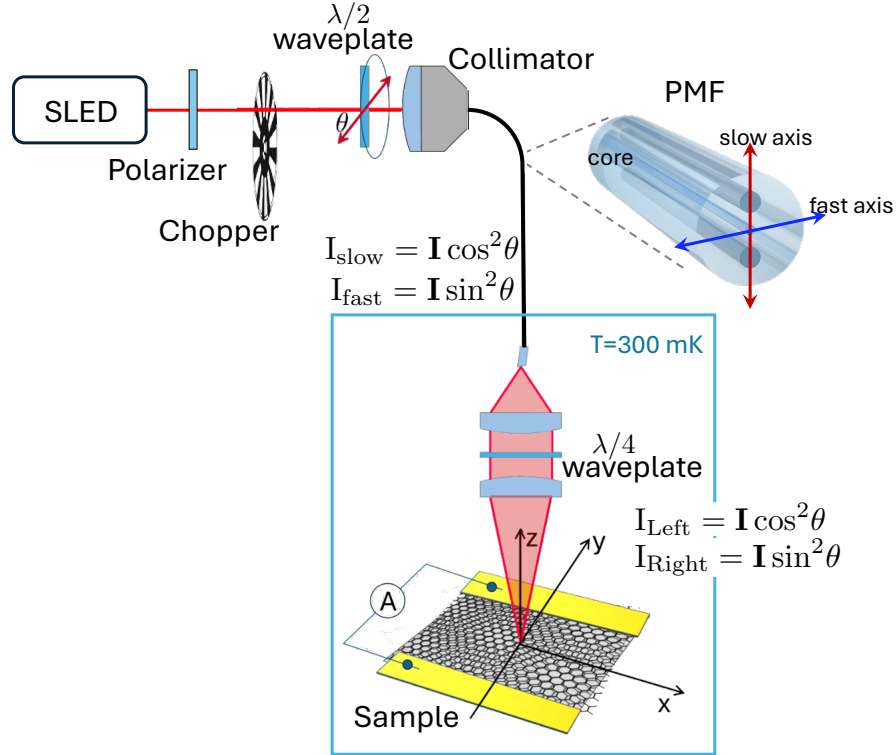


FIG. S1: Cartoon representation of the experimental setup used in this study. Here a 1550nm SLED source shines through polarizer then a chopper

Finite element simulations

We used a modified Shockley-Ramo theorem [14] to calculate the photocurrent collected at the electrodes, as a function of the beam position. The photocurrent is given by

$$I_{ph} = \int d^2r \mathbf{J}_{ph} \cdot \nabla \psi, \quad (\text{S.27})$$

where \mathbf{J}_{ph} is the photo-induced current, and ψ is an auxiliary potential, obtained by solving the Laplace equation $\nabla(\sigma \nabla \psi) = 0$, where σ is the electrical conductivity and the boundary conditions are set such that $\psi = 0$ on the drain electrode and $\psi = 1$ on the source electrode. This ensures that the total current in the device, $\mathbf{J} = -\sigma \nabla V + \mathbf{J}_{ph}$, satisfies the continuity equation $\nabla \cdot \mathbf{J}_{ph} = 0$.

The photo-induced current has two sources: a thermo-electric effect, where $\mathbf{J}_{th} = -S\sigma \nabla T$, where S is the Seebeck coefficient and T is the temperature, and a photogalvanic contribution, where $\mathbf{J}_{CPGE} \propto (i\mathbf{E} \times \mathbf{E}^*)_z \hat{\mathbf{x}}$.

The temperature gradient was estimated by solving a diffusion equation,

$$-\nabla(\kappa \nabla T) + CT = \frac{P}{2\pi w^2} e^{-(\mathbf{r}-\mathbf{r}_0)^2/2w^2}, \quad (\text{S.28})$$

where κ is the thermal conductivity of graphene, C is the thermal coupling between the graphene and we assumed the beam has a Gaussian profile with width w , a total absorbed power P and centered at \mathbf{r}_0 .